Interconversion of intrinsic defects in $SrTiO_3$(001)

S. A. Chambers,[1,*] Y. Du,[1] Z. Zhu,[1] J. Wang,[1] M. J. Wahila,[2] L. F. J. Piper,[2] A. Prakash,[3] J. Yue,[3] B. Jalan,[3] S. R. Spurgeon,[1] D. M. Kepaptsoglou,[4,5,6] Q. M. Ramasse,[4,7,8] and P. V. Sushko[1]

[1]*Pacific Northwest National Laboratory, Richland, Washington 99352, USA*
[2]*Department of Physics, Binghamton University, Binghamton, New York 13902, USA*
[3]*Department of Chemical Engineering and Materials Science, University of Minnesota, Minneapolis, Minnesota 55455, USA*
[4]*SuperSTEM, SciTech Daresbury Campus, Daresbury WA4 4AD, United Kingdom*
[5]*Jeol Nanocentre, University of York, Heslington, York YO10 5BR, United Kingdom*
[6]*Department of Physics, University of York, Heslington, York YO10 5BR, United Kingdom*
[7]*School of Chemical and Process Engineering, University of Leeds, Leeds LS2 9JT, United Kingdom*
[8]*School of Physics, University of Leeds, Leeds LS2 9JT, United Kingdom*

(Received 15 January 2018; revised manuscript received 28 March 2018; published 12 June 2018)

Photoemission features associated with states deep in the band gap of n-$SrTiO_3$(001) are found to be ubiquitous in bulk crystals and epitaxial films. These features are present even when there is little signal near the Fermi level. Analysis reveals that these states are deep-level traps associated with defects. The commonly investigated defects—O vacancies, Sr vacancies, and aliovalent impurity cations on the Ti sites—cannot account for these features. Rather, *ab initio* modeling points to these states resulting from interstitial oxygen and its interaction with donor electrons.

DOI: 10.1103/PhysRevB.97.245204

I. INTRODUCTION

$SrTiO_3$ (STO) is a prototypical oxide semiconductor of considerable interest for oxide electronics. Much effort has been expended to achieve high electron mobilities in bulk and thin-film STO and gain control over STO synthesis with the goal of producing atomically precise material. Inherent in this scientific endeavor is the need to classify and quantify defects and assess their impact on electronic properties. The electronic properties of bulk STO have been extensively studied. Hall data taken for Nb-doped STO at room temperature show that the carrier concentration is typically less than the Nb concentration [1]. High-temperature transport data are typically interpreted in terms of the equilibration of O vacancies (V_O), Sr vacancies (V_{Sr}), aliovalent cation impurities on the Ti site (M_{Ti}), and donor dopants [2–5]. V_{Sr} and M_{Ti} are deep-level acceptors that can trap donor electrons from V_O. Interstitial O (O_{int}) has not been considered in these models because its formation energy is high in fully equilibrated STO crystals [6]. Additionally, a significant literature exists describing the use of undoped (i.e., not intentionally doped) STO crystals as substrates and active channel materials in polar/nonpolar oxide heterostructures, such as the heavily studied $LaAlO_3/SrTiO_3$(001) (LAO/STO) interface. Here, some form of electron transfer results in carriers within the STO. However, it is universally observed that sheet carrier concentration at the interface is an order of magnitude lower than expected based on the electronic reconstruction model [7–9] or a surface defect charge transfer model associated with H adsorption [10]. It is thus important to understand the nature of traps in STO.

Photoemission spectroscopy is an ideal way to directly probe occupied states within the band gap. The absence of background counts from higher kinetic photoelectrons that inelastically scatter endows the method with exquisite sensitivity. For doping levels in the atomic percent range or higher, n-STO exhibits a feature at or slightly below the Fermi level (E_F) associated with photoemission from itinerant electrons from donors. This peak (feature A) has been referred to as the "metallic band." For example, a large metallic band, attributed to a two-dimensional electron gas (2DEG), appears within 10 min when using synchrotron-based soft x rays for photoemission as the intense x-ray beam induces extensive V_O creation in the near-surface region of the crystal [11–14].

Photoemission features have also been observed deeper in the gap for many years and have been appropriately named "in-gap states." These consist of a broad peak $\sim$1−2 eV below E_F (feature A'), which typically appears along with feature A, and a second broad feature tailing off the top of the valence band (VB) (feature B). Feature A' has received considerable attention, but feature B has been discussed very little. Early studies interpreted A' as being due to many-body effects [15]. However, it was pointed out that electron correlation is not sufficiently strong at low doping levels to drive Hubbard band formation [16]. A and A' have also been referred to as "coherent" and "incoherent" states, respectively [17]. "Coherent" denotes that electrons therein are screened by a delocalized band that is coherent with the lattice, whereas electrons in A' are thought to be screened by localized states that some investigators associated with V_O [18]. Ishida *et al.* [17] performed resonant photoemission on $SrNb_xTi_{1-x}O_3$ (Nb:STO, $x = \sim 0.06$) and concluded that electron correlation is not likely to exert a major influence, at least for small x. Rather, it was argued that weak local screening causes A' to

*Corresponding author: sa.chambers@pnnl.gov

split off from A. Resonant photoemission results also reveal that A is largely Ti $3d$ derived whereas A' has mixed Ti $3d$ and O $2p$ character [17,19]. Additionally, resonant photoemission was used to probe the interface electronic structure at conductive LAO/STO heterojunctions. Features analogous to A and A' were observed and assigned to polarization doping and localized V_O states, respectively [18]. Koitzsch *et al.* [19] argue that A' comes from defects of an unspecified nature. While feature B is universally observed, it is rarely commented on. Hatch *et al.* [20] claim that feature B is present only for acid-etched bulk Nb:STO(001) and assigned it to H bound to surface Ti cations. The purpose of this paper is thus to present a detailed experimental and theoretical investigation of feature B, which we find in bulk and epitaxial STO. We find that the most plausible cause of feature B is interstitial O^{2-}.

II. EXPERIMENT AND *AB INITIO* MODELING METHODS

Our investigation is based on bulk crystals of $SrNb_xTi_{1-x}O_{3-\delta}(001)$ ($0 \leqslant x \leqslant 0.03$ with $\delta = 0$, and $0 \leqslant \delta \leqslant 0.023$ with $x = 0$), as well as epitaxial films of $La_{0.01}Sr_{0.99}TiO_3(001)$ prepared using conventional [21] and hybrid molecular beam epitaxy (h-MBE) [22–24]. Measurements were carried out using bulk $SrNb_xTi_{1-x}O_3(001)$ single crystals from MTI and CrysTec with x values ranging from 0 to ~0.03 (1.5 wt %). All crystals were synthesized using the Verneuil method [25]. Polished wafers of dimensions 10 mm × 10 mm × 0.5 mm were prepared on the bench by sonication in acetone and isopropanol to degrease, etching in buffered HF (BHF) for 30 s to dissolve SrO terraces, and rinsing in deionized (DI) water. The wafers were then annealed for 4 h at 1000 °C in an air-filled tube furnace at 1 atm, with 4-h up and down temperature ramps, and rinsed again in DI water. Once under high vacuum in an oxide molecular beam epitaxy (MBE) chamber appended to a UPS/XPS system at PNNL, the crystals were annealed in an electron cyclotron resonance oxygen plasma beam at $\sim 2 \times 10^{-6}$ Torr for 30 min at 650 °C to remove surface contamination. Typical electron diffraction patterns revealing a well-ordered (1 × 1) structure are shown in Fig. 1.

Additional measurements were carried out on a 70-nm-thick La-doped STO film grown by h-MBE on a Nb-doped $SrTiO_3(001)$ substrate. The film was grown in the middle of the Sr-to-Ti beam equivalent pressure ratio space known as the growth window, in which film nucleation is adsorption controlled [22–24]. This deposition procedure ensures optimal film stoichiometry. The La doping level was ~1 at % within the A-site sublattice (e.g., $La_{0.01}Sr_{0.99}TiO_3$).

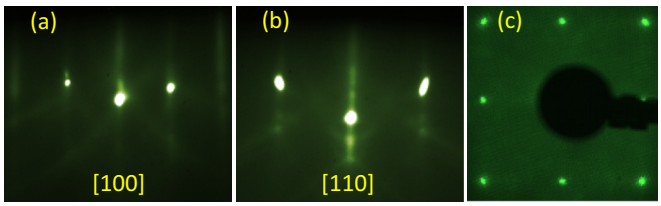

FIG. 1. Reflection (a, b) high-energy electron diffraction (15 keV) and (c) low-energy electron diffraction (69 eV) for n-$SrTiO_3(001)$ after oxygen plasma cleaning.

We have measured VB and gap spectra excited by vacuum ultraviolet (VUV), soft x rays, and synchrotron-based hard x rays. Core-level spectra were also measured with the soft and hard x-ray sources. Conventional UPS and XPS measurements were made at PNNL using monochromatic He I UV light (21.2 eV) and monochromatic Al $K\alpha$ x rays (1487 eV), together with an Omicron/Scienta R3000 analyzer. Measurements on undoped specimens were carried out using a low-energy (2 eV) electron flood gun to neutralize the photoemission charge which forms on the surface and precludes reliable spectral acquisition. Hard x-ray photoemission spectroscopy (HAXPES) measurements were made at the Diamond Light Source (UK) on the I09 Surface and Interface Structural Analysis beamline at an x-ray energy of 6000 eV. This beamline includes an Omicron/Scienta EW4000 high-energy analyzer.

We have also used monochromated valence electron energy loss spectroscopy (VEELS) in a scanning transmission electron microscope. Scanning transmission electron microscopy (STEM) samples were prepared using an as-received undoped STO(001) substrate from CrysTec. We used an FEI Helios NanoLab dual-beam focused ion beam (FIB) microscope and a standard liftout procedure along the STO [100] zone axis, with initial cuts at 30 keV/2° and final polishing at 2 keV/2.5° ion beam energy per incidence angle. Monochromated VEELS measurements were conducted on a Nion UltraSTEM 100MC "Hermes" microscope operating at 60 keV, with a convergence angle of 31 mrad and VEELS collection angles of 19 and 38 mrad. Low-loss data were acquired at several dispersions (5, 10, and 50 meV) with the same effective energy resolution of 16–18 meV set by the monochromator. The data were subsequently aligned to correct for energy drift and the zero-loss peak was removed using reference spectra collected in the vacuum. To explore the effect of retardation losses, low-loss spectra were simulated using the Kröger formula, as implemented in MATLAB by Egerton [26,27]. Simulations were conducted using experimental parameters, a measured bulk plasmon energy of 31.18 eV, and a full width at half maximum (FWHM) of 4.70 eV for sample thicknesses of 5, 10, 25, 50, and 100 nm.

A TOF-SIMS5 time-of-flight secondary ion mass spectrometer made by IONTOF GmbH was used to determine the concentrations of metal impurities in STO crystal from both CrysTec and MTI. A 20-keV Ar_n^+ cluster beam was used for sputtering of an area of 200 × 200 μm^2 and a 25-keV Bi_3^+ beam was used for analysis, which was scanned on an area of 50 × 50 μm^2 at the Ar_n^+ crater center [28].

To model thermodynamic stability, local atomic structures, and electronic properties of defects, the bulk STO was represented using a 4 × 4 × 4 cubic supercell. Relative energies of defect configurations and the corresponding one-electron densities of states were calculated using the Vienna *Ab initio* Simulation Package (VASP) [29,30]. The projector-augmented wave was used to approximate the electron-ion potential [31]. In all cases we used the PBEsol density functional [32], together with a rotationally invariant Hubbard $U_{\text{eff}} = U - J$ correction applied to Ti $3d$ states [33]. The lattice parameter was preoptimized for each value of U_{eff} we considered (0–8 eV), yielding a corresponding range of a_0 (3.89−3.95 Å), and a_0 remained fixed while internal degrees of freedom were fully relaxed in all subsequent calculations. Most calculations were performed

using $U = 4$ eV [34] and a supercell parameter of 15.69 Å, corresponding to the STO lattice parameter $a_0 = 3.92$ Å (less than 0.4% difference from the experimental value of 3.905 Å). We found this approach to provide a reasonable compromise between PBEsol proper, which gives more accurate lattice parameters, and PBEsol + U (with $U = 8$ eV), which yields a more acccurate value of the band gap but overestimates the lattice parameters by ∼1.2%. The plane-wave basis set cutoff of 500 eV was used. The effect of the k-grid was tested for the ideal STO lattice. We found that the difference between total energies calculated at the Γ point only and a Γ-centered $2 \times 2 \times 2$ Monkhorst-Pack grid is less than 2.5 meV per atom. We thus used the Γ point only in all subsequent simulations unless otherwise stated. To model interconversion reactions, we consider all participating defects present simultaneously in the same supercell, as opposed to modeling single defects per supercell. Doing so does not require making assumptions regarding how much of the electron charge is transferred from one defect to another and does not require charge compensation background for charged defects.

III. RESULTS

We find that photoemission intensity appears deep in the gap for all STO specimens investigated, including n-type, undoped, bulk crystals and epitaxial films. These features correspond to the occupied states of deep-level traps that immobilize a significant fraction of itinerant electrons. States closer to E_F become occupied only as the donor concentration increases beyond that required to populate the deep levels.

Representative VB and gap spectra excited with hard and soft x rays, as well as with VUV photons, are shown for bulk Nb:STO(001) in Fig. 2. The different VB shapes reflect differences in cross section at the three photon energies, as well as differences in probe depth. Nevertheless, the leading edges overlap and extrapolations to the energy axis indicate that the valence band maximum (VBM) is ∼3.3 eV below the

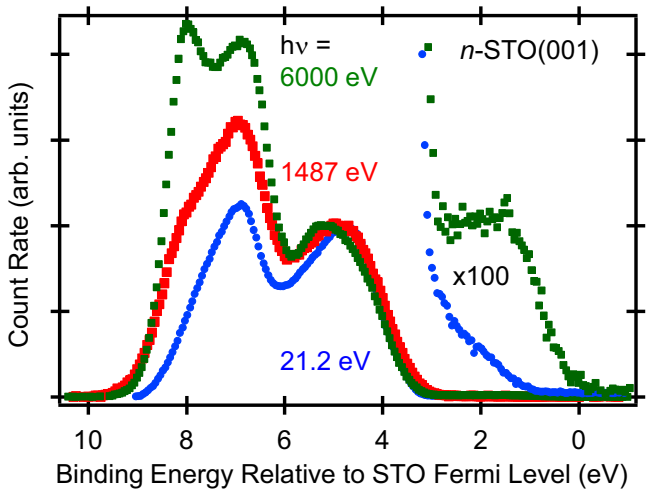

FIG. 2. VB spectra for $SrNb_xTi_{1-x}O_3(001)$ measured at photon energies of 6000 eV with $x = 0.029$, and at 1487 and 21.2 eV with $x = 0.010$ (same sample). The probe depths are ∼1, ∼11, and ∼32 nm for $h\nu = 21.2$, 1487, and 6000 eV.

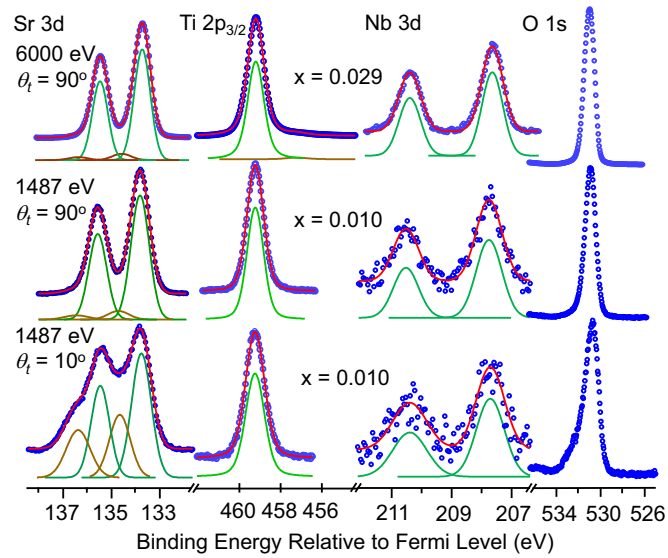

FIG. 3. Core-level photoemission spectra for bulk $SrNb_xTi_{1-x}O_3(001)$ measured at x-ray energies of 6000 and 1487 eV, and at photoelectron take-off angles (θ_t) of 90° (normal emission) and 10° for $h\nu = 1487$ eV.

Fermi level, as expected for flat-band STO. We magnify two of the three gap spectra in the inset of Fig. 2 for which counting statistics in the gap well above the detector dark current can be accumulated due to the high brightness of the respective sources (VUV and hard x ray). There is significant intensity deep in the gap for both spectra, but the count rate rapidly falls off as the Fermi level is approached. Higher count rates deeper in the gap are also nominally detectable in the spectrum excited using the much weaker monochromatic Al $K\alpha$ x-ray (1487 eV) source (not shown due to poor signal-to-background ratio). Using the He I excited VB spectrum as an internal standard, the deep-gap state intensity indicates a deep-level acceptor concentration of a few parts per thousand. We have eliminated the possibility that this deep in-gap intensity is artifactual by comparing with gap spectra from clean p-Ge(001), as described in the Supplemental Material [35].

Core-level analysis reveals that substitutional Nb dopants exhibit a valence of 5+ for both crystals, indicating complete donor ionization. We show in Fig. 3 core-level photoemission spectra to go along with the VB spectra shown in Fig. 2. The Ti $2p$ and Nb $3d$ spectra are well fit using pairs of Voigt functions to represent spin-orbit (SO) coupling. Using these two core levels in conjunction with the relevant atomic cross sections [36,37], x was experimentally determined to be 0.029 and 0.010 for the different crystals measured at 6 and 1.5 keV, respectively. The absolute binding energies indicate a nearly flat-band condition within the two probe depths, defined as the depths at which a photoemission signal originating at the surface would be attenuated by 99.5%. The corresponding numerical value is 5.3λ, where λ is the electron attenuation length. We have estimated λ values specifically for STO by measuring Ge and STO VB intensities for epitaxial STO films grown on Ge(001) and comparing to intensities for phase pure Ge(001) and STO(001). The resulting values are 2 and 6 nm for $h\nu = 1487$ and 6000 eV, respectively [38]. The measured

binding energies are consistent with the presence of majority Ti^{4+} [39] and exclusively Nb^{5+} [40], indicating complete donor ionization. A weak Ti^{3+} shoulder shifted ~2.0 eV to lower binding energy is observed in the crystal measured at 6 keV, consistent with itinerant electrons from ionized Nb donors temporally reducing Ti^{4+} [41]. The Ti^{3+} peak constitutes 2.4% of the total Ti $2p_{3/2}$ peak area, in good agreement with 2.9%, the x value from the Nb $3d$ and Ti $2p$ spectra.

A second pair of SO-split peaks shifted to higher binding energy by ~0.9 eV is required to obtain good fits for the Sr $3d$ spectra. A more surface-sensitive geometry ($\theta_t = 10^\circ$ at $h\nu = 1487$ eV, $5.3\lambda = \sim 1.9$ nm) reveals a substantial increase in the intensity of the higher binding energy Sr $3d$ features, indicating that these photoelectrons originate at the surface. The two most likely surface species that would yield peaks at these binding energies are $Sr(OH)_2$ and SrO_x. If $Sr(OH)_2$ is present, the O $1s$ spectrum is expected to show a well-resolved feature due to OH shifted ~1–2 eV to higher binding energy from the lattice peak, as occurs on bulk CaO(001) [42]. This feature would be more pronounced at $\theta_t = 10^\circ$. However, no such feature is seen. In contrast, the O $1s$ binding energy for SrO_x surface clusters is not expected to be sufficiently different from that of lattice O in STO. The slight asymmetry seen in the O $1s$ spectrum at $\theta_t = 10^\circ$ may be the result of an unresolved SrO_x feature. It has been shown that SrO_x forms on the STO(001) surface as a result of annealing at ~1000 °C in oxygen, as we have done as part of our surface preparation, presumably due to Sr vacancy creation and diffusion to the surface [43,44].

Additionally, the expected Ti^{3+} peak resulting from donor electrons at the bottom of the conduction band (CB) is barely detectable in the Ti $2p$ spectrum taken at 6 keV but is not observable in the spectrum taken at 1487 eV. Yet, our modeling indicates that we should be able to detect Ti^{3+} at the ~1 at %. level. We show in Fig. 4(a) linear combinations of Ti $2p$ spectra measured for lightly doped $SrNb_xTi_{1-x}O_3(001)$ (x = ~0.001) and epitaxial $LaTiO_3(001)$ [45] to simulate spectra for $SrNb_xTi_{1-x}O_3(001)$ with larger x, ranging from 0.01 to 0.10. In the absence of electron trapping defects, each ionized Nb dopant populates the conduction band with one itinerant electron which will, in turn, result in the reduction of a B-site Ti^{4+} cation to Ti^{3+} over the time scale of photoemission (~10^{-16} s). However, donor electrons may also become trapped at defect trap states, if indeed such defects are present. In this case, Ti^{3+} would not appear in the experimental spectrum *unless* the defect has substantial Ti $3d$ character. Assuming defect-free STO, there would be a quantitative transfer of intensity from the Ti^{4+} binding energy in the Ti $2p_{3/2}$ spectrum to the Ti^{3+} binding energy (~1.2 eV lower). This effect would not be as clear in the $2p_{1/2}$ region due to enhanced lifetime broadening resulting from Coster-Kronig decay. In Fig. 4(b), we overlap the simulation for $x = 0.01$ with an actual spectrum for $SrNb_{0.01}Ti_{0.99}O_3(001)$ and plot the difference spectrum. There is clearly a shoulder on the low-binding-energy side of the $2p_{3/2}$ peak in the simulation that does not appear in the measured spectrum. This analysis suggests although the Nb dopants are ionized, resulting in their exhibiting binding energies characteristic of Nb^{5+}, there are not enough itinerant electrons residing at the bottom of the conduction band to modify the Ti $2p$ line shape for $x = 0.01$. This result is consistent with the extreme weakness of a metallic peak in the VB spectrum (see inset to Fig. 2).

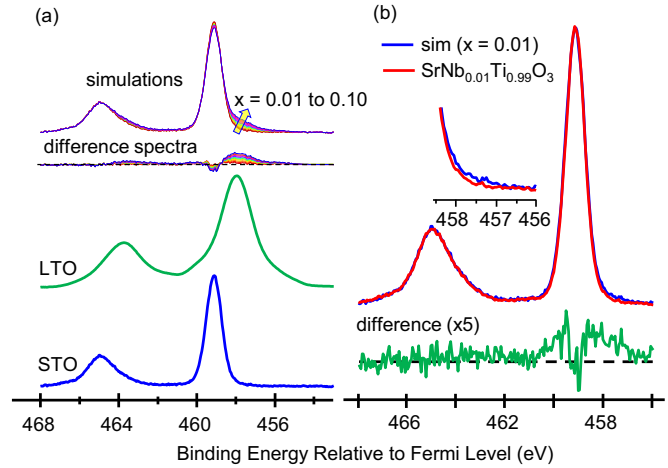

FIG. 4. (a) Simulations of the Ti $2p$ spectrum for $SrNb_xTi_{1-x}O_3$ for $0.01 \leqslant x \leqslant 0.10$ based on the assumption that every Nb donor results in one Ti^{3+} cation, as required for charge neutrality in a defect-free crystal. The simulations are linear combinations of spectra from pure, bulk $SrNb_{0.001}Ti_{0.999}O_3(001)$ and epitaxial $LaTiO_3(001)$. The difference spectra (simulation minus pure STO) show a transfer of intensity from the nominally Ti^{4+} binding energies to that for Ti^{3+} in both spin-orbital channels. (b) Comparison of the simulated and measured spectra for $x = 0.01$.

VEELS measurements provide further evidence for clear intensity deep in the gap of bulk STO crystals. Figures 5(a) and 5(b) show VEELS measurements from regions of varying thickness at two different electron energy loss spectroscopy (EELS) collection angles. We observe a clear intensity plateau in the range 1.5–3.5 eV (marked by the arrow) across all our measurements that is in good qualitative agreement with our photoemission results. However, it is known that valence and low-loss EELS measurements can be influenced by a variety of effects, including the generation of Čerenkov radiation above a particular accelerating voltage, the excitation of guided light modes, and other retardation losses [46]. The Čerenkov limit can be calculated as

$$E_C = 511\left\{\left[\frac{\varepsilon_{1,\max}}{e_{1,\max}-1}\right]^{0.5} - 1\right\}, \qquad (1)$$

which yields ~25–26 keV for $SrTiO_3$ with a maximum dielectric constant of $\varepsilon_{1,\max} \approx 11$ [46]. While the present measurements were performed above this limit at 60 keV accelerating voltage, we note that Erni and Browning [47] have shown that the probability of emitting bulk Čerenkov photons with respect to the maximal emission rate ranges from 0.4 to 0.5 for STO at 60 keV. This value is sufficiently low to expect that it will add only a minimal contribution to the measured data.

To assess the impact of guided light modes and retardation losses as possible additional intensity in the gap region, we have performed simple simulations of low-loss spectra using our experimental parameters for several thicknesses, as shown in Figs. 5(c) and 5(d). These simulations were performed within the Kröger formalism [48], using solely the STO bulk plasmon

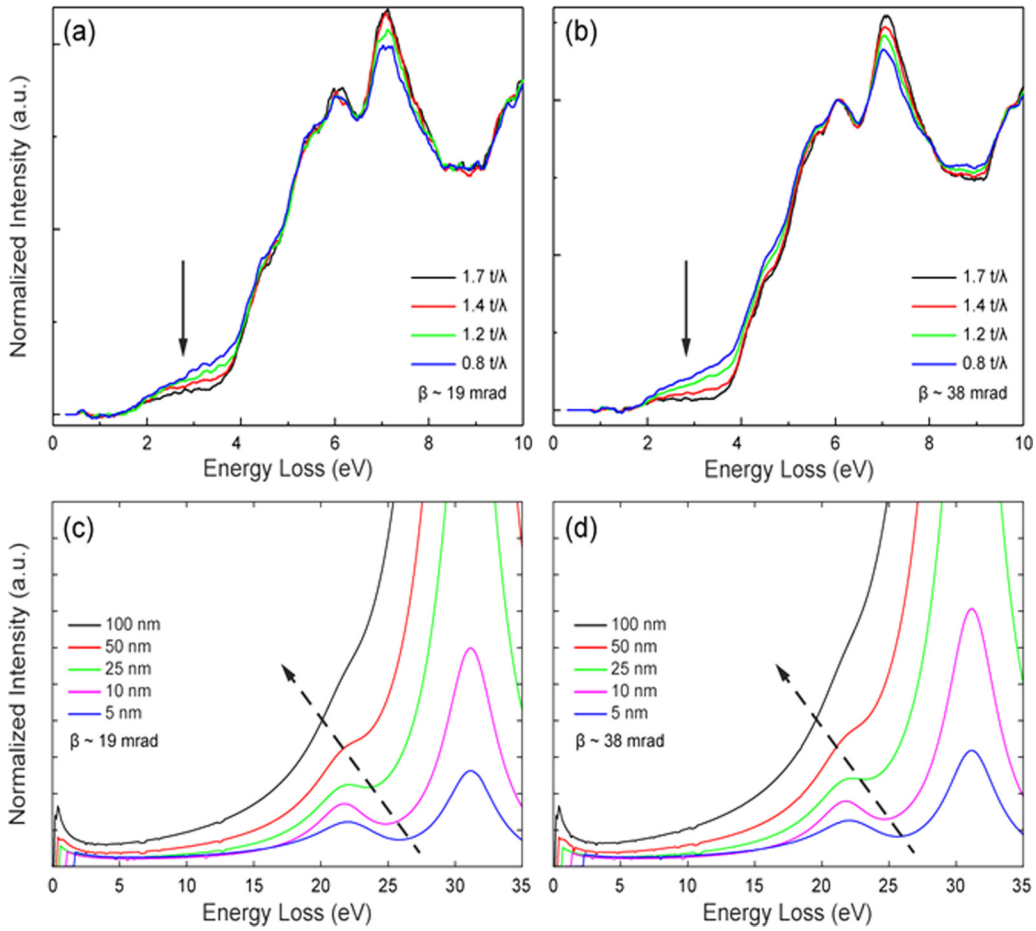

FIG. 5. VEELS measurements conducted with (a) 19 and (b) 38 mrad collection angles (β), respectively, for a range of sample thicknesses. The spectra have been normalized to the signal integral. Simulated low-loss spectra for (c) 19 and (d) 38 mrad collection angles, respectively, for a range of sample thicknesses.

energy of 31.18 eV measured by VEELS as input. While this approach yields identical results to the more rigorous dispersion bracket formalism of Bolton and Chen [49] for single-slab models, the detailed VEELS fine structure (e.g., interband transitions) is not reproduced here, as this would necessitate the use of the dielectric function as input to more rigorous simulation code. Our simulations support two main trends, which have been previously discussed by Erni and Browning [47]: namely, losses due to the excitation of guided light modes lead to the formation of a slight additional background plateau in the gap, which is known to result in an apparent shift in the measured band-gap onset that depends on sample thickness. Experimentally we observe a persistent and sizable gap intensity in even the thinnest parts of our sample, suggesting that guided light modes are likely not responsible for this feature. While we cannot fully exclude the contribution of surface effects without more thorough simulations that are beyond the scope of the present work, our VEELS results lend good qualitative support to the photoemission results described above.

Deep in-gap photoemission is not limited to bulk STO crystals. We also make this observation for epitaxial films deposited using both conventional and hybrid molecular beam epitaxy methods. We show in Fig. 6 spectra for several bulk crystals and MBE-grown epitaxial films over a range of doping levels (less than ~2 at %). A broad feature tailing off the VB (feature B) is observed in all cases, and a feature at ~1 eV (A') is seen for the undoped bulk crystal. In no instance is the feature

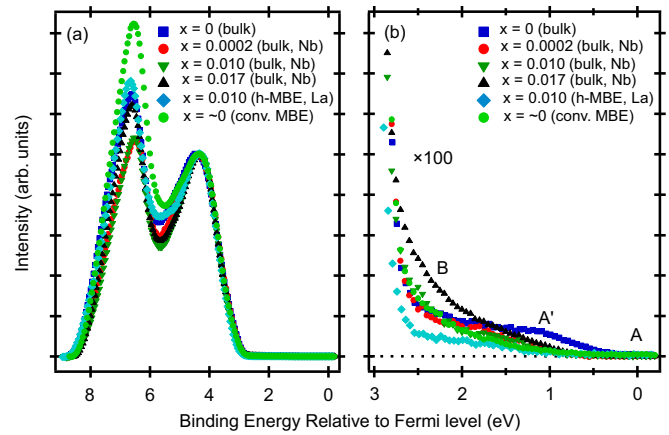

FIG. 6. (a) VB and (b) gap spectra excited with 21.2 eV photons for bulk STO(001) crystals with a range of doping levels, as well as for epitaxial films. A 14-nm film of nominally undoped STO was deposited on p-Ge(001) by conventional MBE. The deposition conditions that were used lead to the incorporation of some V_O. The h-MBE film is 70 nm $La_{0.01}Sr_{0.99}TiO_3$(001) grown on Nb:STO(001).

near the Fermi level (A) of any appreciable magnitude. In all cases, the total integrated intensity in the gap is of the order of parts per thousand of the VB intensity. These results reveal that the deep-level state (B) traps the majority of electrons from donor dopants, but that state B is also occupied for bulk crystals and epitaxial films not intentionally doped. It is noteworthy that in all cases, the core-level binding energies reveal that within the XPS probe depth (∼11 nm), the STO is within ∼0.1 eV of the flat band. Therefore, the populations of A, A', and B are not being affected by band bending, which could sweep carriers into or out of the top few nanometers.

In order to determine how the gap spectrum evolves with dopant concentration in one specific crystal, we utilized an undoped STO(001) crystal as cleaned and after annealing in ultrahigh vacuum (UHV) at progressively higher temperatures and for longer times to generate V_O. The results are shown in the inset to Fig. 7(a). Occupied deep-level states (feature B) are observed prior to vacuum annealing, while the sample is still highly resistive, and the B-state intensities are similar to those measured for doped crystals (see Fig. 6). The intensity of feature B increases modestly through 700 °C, and then increases more substantially at 800 °C. Feature A' gradually strengthens up to 800 °C and strongly increases in intensity at 900 °C. At the same time, a weak shoulder characteristic of Ti^{3+} becomes clearly visible in the Ti $2p$ spectrum at 900 °C, as also seen in Fig. 7(a). These results are consistent with a growing V_O concentration that adds electrons to states in the gap, filling those that are deeper first. From the fit shown in the inset to Fig. 7(a), Ti^{3+} constitutes 4.6% of the total Ti $2p$ peak area after annealing at 900 °C for 60 min, corresponding to a composition of $SrTiO_{2.98}$. Interestingly, the deep-level (B) state drops substantially following the third UHV anneal at 900 °C. A final anneal at 600 °C in activated oxygen has the effect of completely eliminating features A and A' and reducing the intensity of feature B to half the value of the as-cleaned surface.

In Fig. 7(b) we expand the gap spectra overlaid in the inset for Fig. 7(a) and compare these with electronic densities of states (DOS) calculated using an *ab initio* (density functional theory) approach for a set of intrinsic defects [Fig. 7(c)]. We find that V_{Sr} does not result in occupied gap states. However, our calculations show that O_{int}^{2-}, a largely unexplored candidate defect [50], does. We previously found that O_2 is readily absorbed when epitaxial films of $NdTiO_3$ are exposed to air, and that it most likely resides in interstitial sites [51]. The driver is the instability of Ti^{3+}. We now hypothesize that, during the synthesis of bulk and thin-film STO, some vacant anion sites at the crystallization front become occupied by O_2 which traps two electrons. This O_2^{2-} species can be viewed as an interstitial oxygen atom (O_{int}^{0}) bound to a lattice O^{2-} anion (O_{lat}^{2-}) which forms a dumbbell configuration, as shown in Fig. 8(a). Significantly, O_2^{2-} produces no gap states [red DOS in Fig. 7(c)]. Our calculations reveal that in the presence of additional electrons near the bottom of the CB, O_2^{2-} converts to a pair of *separated* interstitial oxygen ions that share three or four electrons and can be represented as $(O-O)^{3-}$ and $(O-O)^{4-}$, respectively, as seen in Fig. 8(b). As the formal charge associated with these species increases from −2 to −3 to $-4|e|$, the distance between the oxygens increases from 1.43 to 1.90 to 2.21 Å. Since the O species in $(O-O)^{4-}$ are

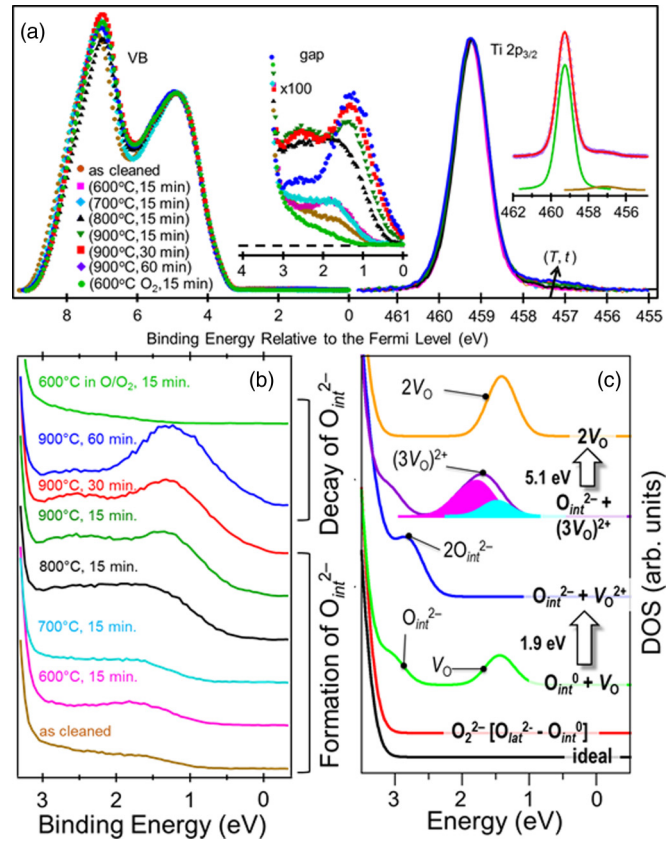

FIG. 7. (a) VB and gap spectra excited with 21.2 eV photons for undoped STO(001) as cleaned and after anneals at 600 °C, 700 °C, 800 °C, and 900 °C in UHV, and one at 600 °C in activated O_2. Also shown are the accompanying Ti $2p_{3/2}$ spectra excited with 1487 eV x rays. Insets: Expanded gap spectra (left) and a fit to Voigt functions (red) for the spectrum measured after the third anneal at 900 °C (right). Slight changes in binding energy caused by variations in band bending (within ∼0.15 eV of flat band) have been removed to facilitate comparison. (b) Expanded view of experimental gap spectra. (c) Calculated DOS for select defect configurations broadened with Gaussian functions using a width of 0.5 eV. This panel shows how the DOS transform as a result of the defect reactions shown to the right. The solid magenta and solid cyan features in the purple DOS result from localized and delocalized electrons from V_O, respectively. The numbers by the arrows are the energies gained in the indicated defect conversion reactions.

equivalent and neither is at a lattice site, we refer to $(O-O)^{4-}$ as a pair of interstitial O_{int}^{2-} ions. As seen in Fig. 8(b), $(O-O)^{4-}$ straddles a V_O^{++} site. If one O_{int}^{2-} diffuses away, the other would occupy the V_O^{++} lattice site and become O_{lat}^{2-}. Significantly, both $(O-O)^{3-}$ and $(O-O)^{4-}$ generate occupied states above the VBM, as seen in the green DOS, depending on their charge states and proximity to other defects. The energy difference between these states and the VBM increases with increasing U_{eff}, reaching ∼1 eV for $U_{eff} = 4$ eV. These interstitial oxygen anions could thus be the deep-level traps we observe. The spin density map for a $2\ O_{lat}^{2-}$–$[3 \times V_O]^2$ defect complex is shown in Fig. 8(c).

To understand the observed evolution of the gap spectrum with annealing, we consider several defect interconversion reactions that involve V_O and O_{int}^{2-} (see green DOS) as well

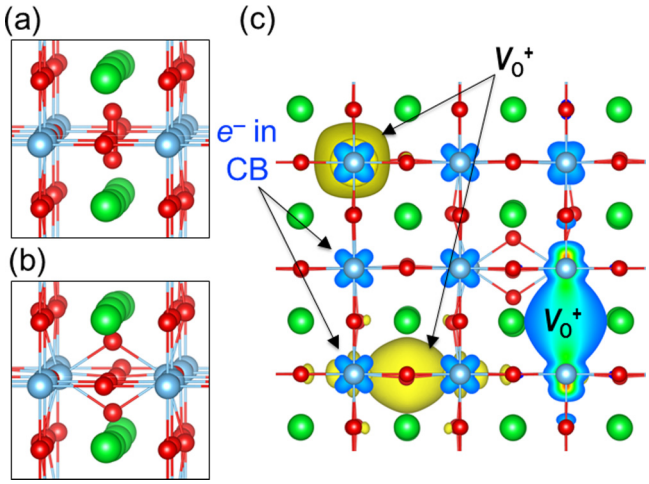

FIG. 8. (a) Local structures for O_2 at an empty anion site (O_2^{2-}) and (b) a pair of O_{int}^{2-} that result from O_2^{2-} trapping $2e^-$ from nearby V_O and dissociating; Sr, Ti, and O are shown as green (large), blue (medium), and red (small) spheres. (c) Surfaces of constant spin density for the $2O_{int}^{2-} + [3 \times V_O]^{2+}$ configuration indicate that three electrons are localized in V_O^+ and one electron is at the conduction-band minimum.

as O_2^{2-}, which is also present in the supercell associated with the green DOS but does not generate any gap intensity. First, we note that the calculated V_O formation energy with respect to $^1/_2O_{2(g)}$ (5.5 eV) decreases to 3.6 eV in the presence of O_2^{2-}. This decrease is driven by the energy gained from O_2^{2-} trapping V_O electrons located near the CB minimum (1.9 eV) and the subsequent dissociation of O_2^{2-} into a pair of O_{int}^{2-} ions. The corresponding DOS change is shown in the transition from green to blue in Fig. 7(c). Since $U_{eff} = 4$ eV corresponds to a one-electron gap value of only 2.3 eV, the effect of O_2^{2-} on the V_O formation energy is underestimated. While the resulting V_O^{++} can recombine with O_{int}^{2-} with an energy gain of 5.1 eV, the electrostatic interaction of these defects can be effectively screened by the lattice, thereby suppressing recombination [52].

As the temperature and anneal duration increase, the concentration of V_O increases as well. In addition to being trapped at O_{int}^{2-}, electrons from these vacancies can be redistributed to V_O^{++} formed previously, leading to partially charged oxygen vacancy complexes V_O^{Q+} ($0 < Q < 2$). To model this scenario, we considered supercells with one O_2^{2-} coexisting with up to three V_O. Two electrons provided by these V_O drive the formation of a pair of O_{int}^{2-}, as discussed above. The other electrons remain at the vacancies. Thus, depending on the V_O concentration, the supercell could contain $[1 \times V_O]^{2+}$, $[2 \times V_O]^{2+}$ or $[3 \times V_O]^{2+}$ defect complexes which have a collective charge of +2 with respect to the lattice.

The purple DOS in Fig. 7(c) shows that, as the V_O concentration increases, so does the intensity of feature A' located ~1.6 eV above the top of the VB. Analysis of the spatial distribution of one-electron bands indicates that, in the case of $[3 \times V_O]^{2+}$, three of the four electrons not bound to $(O_{int})^{2-}$ are localized at the three vacancy sites, resulting in $3V_O^+$, while the fourth electron is delocalized at the CB minimum, as shown by the spin densities in Fig. 8(c). We note that three oxygen vacancies per 64 unit cells, which correspond to ~1.56% of the oxygen lattice site, is reasonably close to the actual oxygen vacancy concentration in the crystal following UHV annealing (~ 0.7%). A similar distribution is found for $[2 \times V_O]^{2+}$. These localized and delocalized bands map well onto the experimentally observed midgap band at ~1.4 eV which has a long trail running up to E_F, as seen by comparing Figs. 7(b) and 7(c). We note that the band gap is underestimated for $U_{eff} = 4$ eV. Thus, the delocalized band (cyan) is too close in energy to the localized V_O^+ band (magenta). The gold DOS shows that when all O_{int}^{2-} and V_O^{Q+} diffuse and recombine, V_O and a 5.1-eV energy gain are the results.

We note that the lattice deformation field induced by each defect affects the geometrical and electronic structure of all other defects located within the same supercell. These effects are explicitly included in our calculations through relaxation of the internal degrees of freedom. This interaction contributes to broadening of the corresponding density of state features to an extent that depends on the distance between the defects, and their spatial configurations. However, analysis of the DOS (see Fig. S2 in the Supplemental Material [35]), calculated for four types of defects in $2 \times 2 \times 2$ and $4 \times 4 \times 4$ supercells, reveals that such defect-defect interaction does not affect our conclusions.

These modeling results allow us to interpret the experimental evolution of the gap spectrum as follows. As the V_O concentration increases, some interstitial oxygens are converted from O_2^{2-} to O_{int}^{2-}, depending on the V_O concentration, and the intensity of the B feature saturates. Prolonged annealing promotes diffusion of O_{int}^{2-} and V_O^{++}. Recombination of these defects to generate O_{lat}^{2-} results in a decrease in the B feature, as observed after 60 min at 900 °C in UHV, while the A and A' features continue to grow. The final anneal in activated oxygen not only eliminates all V_O-derived states but also significantly reduces the concentration of O_{int}^{2-} by means of recombination of O_{int}^{2-} and V_O^{++} in the absence of V_O creation.

IV. DISCUSSION

We now consider other candidate defects as the cause of the deep in-gap states. There is a significant body of literature focused on electronic properties of bulk STO and the associated interpretation based on various defect models. Specifically, high-temperature conductivity as a function of oxygen partial pressure has been modeled using only V_{Sr} and V_O, along with aliovalent metal impurities on the Ti site (M_{Ti}) that act as acceptors, and donors such as La_{Sr} and Nb_{Ti} [2–5]. Ti vacancies have not been included due to their high formation energies [53].

We have investigated whether V_{Sr} can account for the deep in-gap photoemission feature and have concluded that it cannot for the following reasons. First, V_{Sr} DOS are either in the gap and not occupied, or not in the gap and occupied. Indeed, the DOS feature associated with the neutral V_{Sr} (i.e., Sr^{2+} vacancy that has not trapped electrons) is clearly visible close to the top of the VB in Figs. 9(a) and 9(b). Simulations conducted using PBEsol and a hybrid density functional HSE [54] are consistent in predicting the position of this feature with respect to the band edges. However, the absence of electrons at this defect precludes detection by photoemission. Once V_{Sr} traps donor electrons (either one or two), the now occupied V_{Sr} DOS

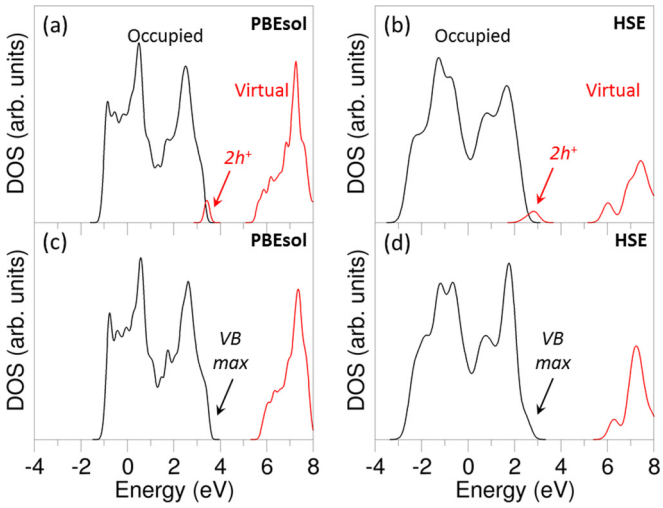

FIG. 9. Densities of states calculated (a, b) for the neutral Sr vacancy and (c, d) for the Sr vacancy with two trapped electrons using (a, c) PBEsol and (b, d) HSE density functionals. The unoccupied states near the top of the valence band are marked with h^+ (a, b). Upon trapping two electrons per Sr vacancy, these states become occupied and produce a small perturbation of the DOS near the VB maximum (c, d), but do not create an in-gap state.

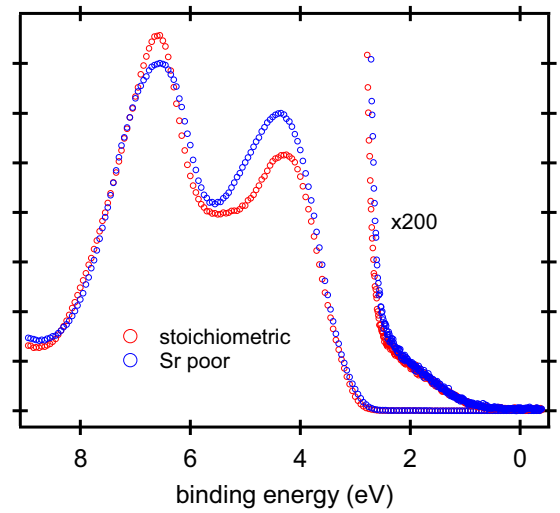

FIG. 10. Comparison of VB and gap spectra for stoichiometric and ∼10% Sr poor STO homoepitaxial films grown by hybrid MBE.

merges with the VB DOS, as shown in Figs. 9(c) and 9(d), so that the perturbation induced by V_{Sr} is not distinguishable from the VB DOS as a whole.

Second, the intensity of the deep in-gap state indicates that the concentration of the causal defect is orders of magnitude higher than the expected concentration of V_{Sr}. De Souza [55] has estimated $[V_{Sr}]$ to be $\sim 5 \times 10^{17}$ cm^{-3} in bulk STO that has been annealed to high temperature in oxidizing conditions, as STO typically is during substrate preparation. Moreover, epitaxial STO films grown using hybrid MBE with the same processing conditions as the stoichiometric film used in this study have been shown by positron annihilation measurements to possess a $[V_{Sr}]$ in the low 10^{16} cm^{-3} range [56]. However, the concentration of the defect that causes the deep in-gap feature in hybrid MBE-grown films is estimated to be at least $\sim 5 \times 10^{19}$ cm^{-3} and at least $\sim 3 \times 10^{20}$ cm^{-3} in bulk STO [57].

Third, the gap spectrum measured for a hybrid MBE film that was deposited on the Sr-poor side of the growth window by a substantial amount is virtually the same as that for the stoichiometric film. We show these results in Fig. 10. Despite a ∼10% Sr deficiency, the nonstoichiometric STO film exhibits virtually the same gap spectrum as the stoichiometric film.

Fourth, there is no correlation between the intensity of the deep in-gap feature and the amount of SrO_x on the STO surface. It is well known that high-temperature annealing of bulk STO in an oxidizing environment leads to Sr vacancy creation and diffusion of Sr to the surface, followed by oxidation to form SrO_x [43]. Moreover, the vapor pressure of SrO is negligible at typical annealing temperatures in STO wafer preparation (∼ 1000 °C), precluding desorption of SrO from the surface during annealing. There should therefore be a direct dependence of the deep in-gap state intensity on the fraction of Sr 3*d* intensity associated with SrO_x (see Fig. 3), if indeed the deep state is caused by V_{Sr}. However, there is no correlation whatsoever between these two quantities in the annealing experiment on undoped STO summarized in Fig. 7. The absence of a correlation is clearly seen in Fig. 11. The first data point is for the undoped STO crystal after cleaning the activated oxygen at 600 °C to remove adventitious carbon. As the UHV annealing continues at progressively higher temperatures from points 2 to 5, the deep in-gap intensity increases monotonically. However, the SrO_x fraction first decreases from point 1 to point 2, and then increases up to point 5, although not in a way that would indicate a correlation. From points 5 to 7, the deep-state intensity drops but the SrO_x fraction increases. Finally, after the second anneal in activated oxygen (point 8), the SrO_x fraction returns to its original value, but the deep-state intensity is considerably smaller.

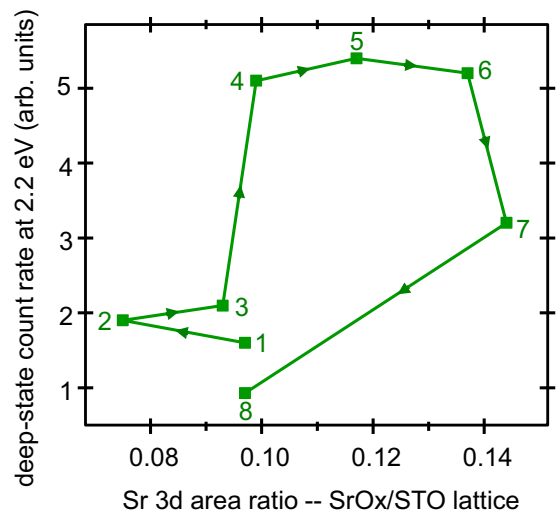

FIG. 11. Deep in-gap state count rate plotted against the SrO_x peak area normalized to the lattice peak area taken from Sr 3*d* spectra for the annealing sequence for undoped STO(001) summarized in Fig. 3. The numbers indicate the steps in the annealing sequence shown in Fig. 3(a).

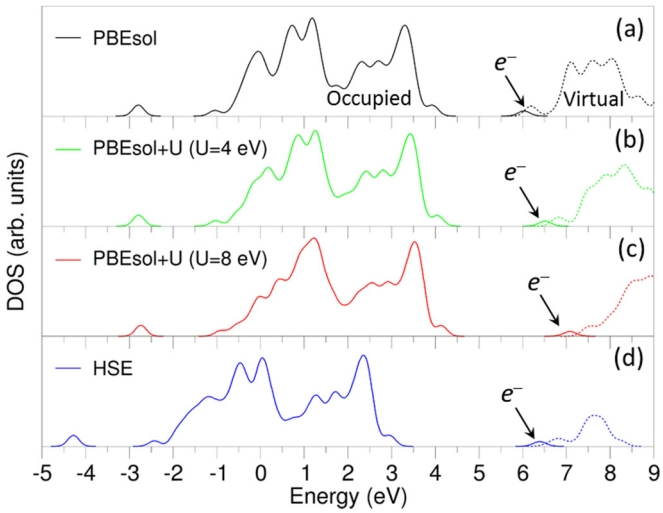

FIG. 12. Densities of states calculated for a hydrogen atom trapped in $SrTiO_3$. The H atom binds to a lattice oxygen, forming an OH^- species and an electron that occupies a state close to the bottom of the CB. DOS calculated using (a) PBEsol and (b) PBEsol + U for $U_{Ti} = 4$ eV and (c) $U_{Ti} = 8$ eV indicate that this electron state is degenerate with the CB minimum. This electronic structure is further supported by the DOS obtained using single-point HSE calculation for the structure preoptimized using (d) PBEsol + U ($U_{Ti} = 8$ eV).

We also investigated the possibility that the deep-gap feature is associated with a hydrogen atom that binds to lattice O^{2-} producing OH^- and an electron. The reaction $O^{2-} + H^0 \rightarrow OH^- + e^-$ is known to produce in-gap localized electronic states in wide-band-gap oxides, such as MgO [58,59] and $12CaO \cdot 7Al_2O_3$ [60]. Here we investigated the electronic structure of the $OH^- + e^-$ configuration using the PBEsol + U density functional with U values of 0, 4, and 8 eV. In all cases the internal coordinates of the systems were optimized, while the lattice parameters were held at the experimental value (3.905 Å). The corresponding DOS are shown in Figs. 12(a)–12(c). As the U value and the calculated band gap increase, the occupied electron state remains close to the bottom of the CB. Additionally, the geometrical configuration preoptimized with $U = 8$ eV was used to calculate the DOS at the HSE level. In this case, the resulting occupied state also fell near the bottom of the conduction band, as shown in Fig. 12(d). Hence, we rule out the presence of an H atom in the bulk of STO as a potential candidate for the deep in-gap feature.

A previous observation of deep in-gap intensity excited with He I UV light ($h\nu = 21.2$ eV) was interpreted as being due to hydrogenation of the surface, resulting in H bound to undercoordinated Ti cations in the terminal layer [20]. These authors note that this feature is seen only for Nb:STO(001) bulk crystals that were etched in either HF or a HCl/HNO_3 mixture, but not for MBE-grown films. In contrast, we see a deep feature in the gap spectra of bulk crystals as well as MBE-grown films. Moreover, our observations were made at photon energies ranging from 21.2 to 6000 eV, indicating that this feature is present in the bulk as well as on the surface. Hatch *et al.* also reported that their deep feature does not disperse in angle-resolved measurements. First-principles modeling reported in Ref. [20] shows that surface H bound to Ti cations does indeed result in a nondispersing feature in the lower portion of the gap, as observed. While we cannot rule out the possibility that some H-Ti is present on the surfaces of our HF-etched bulk crystals and contributes to the signal measured in the lower portion of the gap in these cases, our data clearly show that intensity is also present in epitaxial films that were not acid etched, and in the bulk, as well as on the surface, of all samples examined. We thus rule out surface-bound H-Ti as the sole explanation for the deep in-gap feature. Rather, we think that the feature associated with surface H-Ti overlaps that resulting from bulk O_{int}^{2-} ions when the former is present. We also note that Hatch *et al.* reported that their deep in-gap feature does not change with temperature up to 875 °C. In contrast, ours undergoes a clear evolution over the same temperature range, as described in detail in this article.

Cation impurities which might act as deep-level acceptors in bulk STO crystals are not present in sufficient quantities to be the cause of the deep-level traps. Time-of-flight secondary ion mass spectrometry sputter profiles of representative crystals reveal that Al, Na, Ca, and Mg are present at levels of a few parts per million (ppm) and Si (which is isovalent with Ti and therefore not expected to be a deep-level acceptor) is present at a concentration of ~150 ppm. These concentrations are orders of magnitude lower than that associated with the deep-level gap states (parts per thousand). These in-gap states bear some resemblance to deep subgap states observed in amorphous InGaZnO and ascribed to disorder in the coordination sphere of O [61,62]. However, the origin of the in-gap states in STO is quite different, as discussed above.

Finally, we consider the effect that these deep-level traps have on transport properties. We would expect that measured carrier densities would be lower than donor dopant concentrations if itinerant electrons become trapped in these states. Such appears to be the case. In Fig. 13 we show room-temperature Hall effect measurements for an MTI crystal for $SrNb_{0.015}Ti_{0.985}O_3(001)$. Based on the composition, the expected carrier concentration is 2.52×10^{20} cm^{-3}, assuming 100% ionization of all Nb donors. The measured carrier concentration is 1.84×10^{20} cm^{-3}, 73% of the expected value. A similar observation was also made by Spinelli *et al.* [1]. The measured mobility is 7.75 cm^2/(V s). These results are consistent with the conclusions drawn from analysis of the photoemission and energy loss data.

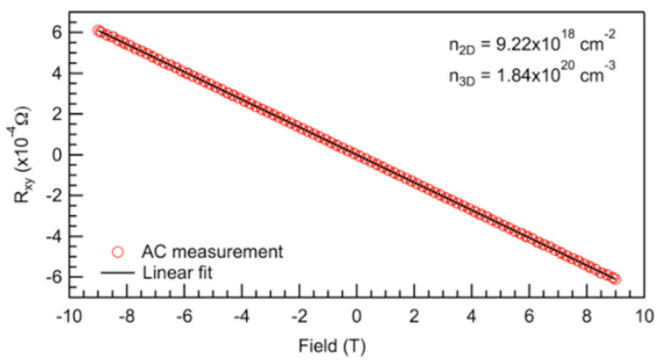

FIG. 13. Hall effect measurement measured at room temperature for a $SrNb_{0.015}Ti_{0.985}O_3(001)$ crystal from MTI.

V. CONCLUSION

We have shown that deep in-gap states of $SrTiO_3(001)$ bulk crystals and epitaxial films result from traps associated with intrinsic defects. The concentration is of the order of parts per thousand, precluding their direct measurement by most techniques. However, combining UPS, XPS, and VEELS spectra with *ab initio* simulations allows us to identify plausible candidates responsible for the deep-gap and midgap bands and to suggest defect interconversion mechanisms that explain the temperature-dependent transformation of the gap spectrum. Moreover, the proposed model suggests an approach to eliminating the deep-gap feature through judicious thermal treatment, thus paving a way to better control of the electronic structure in $SrTiO_3$.

ACKNOWLEDGMENTS

The work was supported by the U.S. Department of Energy, Office of Science, Division of Materials Sciences and Engineering under Award No. 10122 and was performed in the Environmental Molecular Sciences Laboratory, a national scientific user facility sponsored by the Department of Energy's Office of Biological and Environmental Research and located at PNNL. M.J.W. and L.F.J.P. acknowledge support from the National Science Foundation under Grant No. DMR 1409912. We thank the Diamond Light Source for access to beamline I09 (NT16630) and Dr. Tien-Lin Lee for his assistance with the experiments. The BU work was supported by the Air Force Office of Scientific Research under Award No. FA9550-18-1-0024. The work at UMN was funded by the U.S. Department of Energy through the University of Minnesota Center for Quantum Materials, under Grant No. DE-SC-0016371. A.P. acknowledges the support from the UMN Doctoral Dissertation Fellowship. Electron microscopy was carried out at the SuperSTEM Laboratory, the U.K. National Research Facility for Advanced Electron Microscopy, which is supported by the Engineering and Physical Sciences Research Council.

[1] A. Spinelli, M. A. Torija, C. Liu, C. Jan, and C. Leighton, Phys. Rev. B **81**, 155110 (2010).
[2] R. Moos and K. H. Hardtl, J. Am. Ceram. Soc. **80**, 2549 (1997).
[3] R. A. De Souza, V. Metlenko, D. Park, and T. E. Weirich, Phys. Rev. B **85**, 174109 (2012).
[4] R. Meyer, A. F. Zurhelle, R. A. De Souza, R. Waser, and F. Gunkel, Phys. Rev. B **94**, 115408 (2016).
[5] P. C. Bowes, J. N. Baker, J. S. Harris, B. D. Behrhorst, and D. L. Irving, Appl. Phys. Lett. **112**, 022902 (2018).
[6] A. Samanta, E. Weinan, and S. B. Zhang, Phys. Rev. B **86**, 195107 (2012).
[7] A. Ohtomo and H. Y. Hwang, Nature (London) **427**, 423 (2004).
[8] S. Thiel, G. Hammerl, A. Schmehl, C. W. Schneider, and J. Mannhart, Science **313**, 1942 (2006).
[9] M. Huijben, A. Brinkman, G. Koster, G. Rijnders, H. Hilgenkamp, and D. H. A. Blank, Adv. Mater. **21**, 1665 (2009).
[10] P. Scheiderer, F. Pfaff, J. Gabel, M. Kamp, M. Sing, and R. Claessen, Phys. Rev. B **92**, 195422 (2015).
[11] W. Meevasana, P. D. C. King, R. H. He, S. K. Mo, M. Hashimoto, A. Tamai, P. Songsiriritthigul, F. Baumberger, and Z. X. Shen, Nat. Mater. **10**, 114 (2011).
[12] A. F. Santander-Syro, O. Copie, T. Kondo, F. Fortuna, S. Pailhes, R. Weht, X. G. Qiu, F. Bertran, A. Nicolaou, A. Taleb-Ibrahimi, P. Le Fevre, G. Herranz, M. Bibes, N. Reyren, Y. Apertet, P. Lecoeur, A. Barthelemy, and M. J. Rozenberg, Nature (London) **469**, 189 (2011).
[13] Z. Wang, S. M. Walker, A. Tamai, Y. Wang, Z. Ristic, F. Y. Bruno, A. de la Torre, S. Ricco, N. C. Plumb, M. Shi, P. Hlawenka, J. Sanchez-Barriga, A. Varykhalov, T. K. Kim, M. Hoesch, P. D. C. King, W. Meevasana, U. Diebold, J. Mesot, B. Moritz, T. P. Devereaux, M. Radovic, and F. Baumberger, Nat. Mater. **15**, 835 (2016).
[14] S. Gonzalez, C. Mathieu, O. Copie, V. Feyer, C. M. Schneider, and N. Barrett, Appl. Phys. Lett. **111**, 181601 (2017).
[15] Y. J. Chang, A. Bostwick, Y. S. Kim, K. Horn, and E. Rotenberg, Phys. Rev. B **81**, 235109 (2010).
[16] A. Fujimori, I. Hase, M. Nakamura, H. Namatame, Y. Fujishima, Y. Tokura, M. Abbate, F. M. F. de Groot, M. T. Czyzyk, J. C. Fuggle, O. Strebel, F. Lopez, M. Domke, and G. Kaindl, Phys. Rev. B **46**, 9841 (1992).
[17] Y. Ishida, R. Eguchi, M. Matsunami, K. Horiba, M. Taguchi, A. Chainani, Y. Senba, H. Ohashi, H. Ohta, and S. Shin, Phys. Rev. Lett. **100**, 056401 (2008).
[18] G. Berner, M. Sing, H. Fujiwara, A. Yasui, Y. Saitoh, A. Yamasaki, Y. Nishitani, A. Sekiyama, N. Pavlenko, T. Kopp, C. Richter, J. Mannhart, S. Suga, and R. Claessen, Phys. Rev. Lett. **110**, 247601 (2013).
[19] A. Koitzsch, J. Ocker, M. Knupfer, M. C. Dekker, K. Dorr, B. Buchner, and P. Hoffmann, Phys. Rev. B **84**, 245121 (2011).
[20] R. C. Hatch, K. D. Fredrickson, M. Choi, C. W. Lin, H. Seo, A. B. Posadas, and A. A. Demkov, J. Appl. Phys. **114**, 103710 (2013).
[21] S. A. Chambers, Y. Comes, S. R. Spurgeon, and P. V. Sushko, Appl. Phys. Lett. **110**, 082104 (2017).
[22] B. Jalan, P. Moetakef, and S. Stemmer, Appl. Phys. Lett. **95**, 032906 (2009).
[23] B. Jalan, J. Cagnon, T. E. Mates, and S. Stemmer, J. Vac. Sci. Technol. A **27**, 1365 (2009).
[24] T. Q. Wang, K. Ganguly, P. Marshall, P. Xu, and B. Jalan, Appl. Phys. Lett. **103**, 212904 (2013).
[25] C. Rodenbucher, M. Luysberg, A. Schwedt, V. Havel, F. Gunkel, J. Mayer, and R. Waser, Sci. Rep. **6**, 32250 (2016).
[26] R. F. Egerton, *Electron Energy-Loss Spectroscopy in the Electron Microscope* (Springer, New York, 2012).
[27] K. van Bentham, C. Elsasser, and R. H. French, J. Appl. Phys. **90**, 6156 (2001).
[28] Z. Y. Wang, B. W. Liu, E. W. Zhao, K. Jin, Y. G. Du, J. J. Neeway, J. V. Ryan, D. H. Hu, K. H. L. Zhang, M. N. Hong, S. Le Guernic, S. Thevuthasan, F. Y. Wang, and Z. H. Zhu, J. Am. Soc. Mass Spectrom. **26**, 1283 (2015).
[29] G. Kresse and J. Furthmuller, Phys. Rev. B **54**, 11169 (1996).
[30] G. Kresse and J. Hafner, Phys. Rev. B **49**, 14251 (1994).

[31] P. E. Blochl, Phys. Rev. B **50**, 17953 (1994).
[32] J. P. Perdew, A. Ruzsinszky, G. I. Csonka, O. A. Vydrov, G. E. Scuseria, L. A. Constantin, X. L. Zhou, and K. Burke, Phys. Rev. Lett. **100**, 136406 (2008).
[33] S. L. Dudarev, G. A. Botton, S. Y. Savrasov, C. J. Humphreys, and A. P. Sutton, Phys. Rev. B **57**, 1505 (1998).
[34] A. Lopez-Bezanilla, P. Ganesh, and P. B. Littlewood, APL Mater. **3**, 100701 (2015).
[35] See Supplemental Material at http://link.aps.org/supplemental/10.1103/PhysRevB.97.245204 for information on sample preparation, photoemission, electron energy loss and Hall effect measurements, and *ab initio* modeling.
[36] J. H. Scofield, Lawrence Livermore National Laboratory, Report No. UCRL-51326 (1973).
[37] J. J. Yeh and I. Lindau, At. Data Nucl. Data Tables **32**, 1 (1985).
[38] S. A. Chambers, P. V. Sushko, Y. Du, S. R. Spurgeon, M. E. Bowden, J. M. Ablett, T.-L. Lee, N. F. Quackenbush, and J. C. Woicik (unpublished).
[39] S. A. Chambers, T. Ohsawa, C. M. Wang, I. Lyubinetsky, and J. E. Jaffe, Surf. Sci. **603**, 771 (2009).
[40] T. Hadamek, A. B. Posadas, A. Dhamdhere, D. J. Smith, and A. A. Demkov, J. Appl. Phys. **119**, 095308 (2016).
[41] M. S. J. Marshall, D. T. Newell, D. J. Payne, R. G. Egdell, and M. R. Castell, Phys. Rev. B **83**, 035410 (2011).
[42] P. Liu, T. Kendelewicz, G. E. Brown, G. A. Parks, and P. Pianetta, Surf. Sci. **416**, 326 (1998).
[43] K. Szot, W. Speier, U. Breuer, R. Meyer, J. Szade, and R. Waser, Surf. Sci. **460**, 112 (2000).
[44] D. Kobayashi, H. Kumigashira, M. Oshima, T. Ohnishi, M. Lippmaa, K. Ono, M. Kawasaki, and H. Koinuma, J. Appl. Phys. **96**, 7183 (2004).
[45] P. Scheiderer, M. Schmitt, J. Gabel, M. Zapf, M. Stübinger, P. Schütz, L. Dudy, C. Schlueter, T.-L. Lee, M. Sing, and R. Claessen, Adv. Mater. 1706708 (2018).
[46] R. Erni, Ultramicroscopy **160**, 80 (2016).
[47] R. Erni and N. D. Browning, Ultramicroscopy **108**, 84 (2008).
[48] E. Kroger, Z. Phys. **216**, 115 (1968).
[49] J. P. R. Bolton and M. Chen, Ultramicroscopy **60**, 247 (1995).
[50] H. Donnerberg and A. Birkholz, J. Phys.: Condens. Matter **7**, 327 (1995).
[51] P. Xu, Y. Ayino, C. Cheng, V. S. Pribiag, R. B. Comes, P. V. Sushko, S. A. Chambers, and B. Jalan, Phys. Rev. Lett. **117**, 106803 (2016).
[52] R. B. Comes, P. V. Sushko, S. M. Heald, R. J. Colby, M. E. Bowden, and S. A. Chambers, Chem. Mater. **26**, 7073 (2014).
[53] M. J. Akhtar, Z. U. N. Akhtar, R. A. Jackson, and C. R. A. Catlow, J. Am. Ceram. Soc. **78**, 421 (1995).
[54] A. V. Krukau, O. A. Vydrov, A. F. Izmaylov, and G. E. Scuseria, J. Chem. Phys. **125**, 224106 (2006).
[55] R. A. De Souza, Adv. Funct. Mater. **25**, 6326 (2015).
[56] D. J. Keeble, B. Jalan, L. Ravelli, W. Egger, G. Kanda, and S. Stemmer, Appl. Phys. Lett. **99**, 232905 (2011).
[57] These concentrations were determined by using the VB spectrum as an internal standard. Because the VB of STO is mostly O $2p$ derived, the total VB intensity is to first approximation proportional to $3\sigma_{O2p}$, where σ_{O2p} is the O $2p$ photoemission cross section and the constant of proportionality depends on the instrument response function and the photoelectron attenuation length. Likewise, the total intensity of the deep in-gap feature is proportional to $x\sigma_{\text{deep gap}}$, where x is the mole fraction of the causal defect, $\sigma_{\text{deep gap}}$ is the associated photoemission cross section, and the constant of proportionality is essentially the same as that for the VB. The largest uncertainty in this approach is that we do not know what cross section to use for the deep in-gap state because the identity of the causal defect cannot be determined by independent means. However, because the largest cross-section estimate will result in the lowest defect concentration, we use the largest conceivable value in order to determine the lower limit of the concentration of the causal defect. Of the different species that can reasonably be assigned as causing the deep state (Sr, Ti, O, H, or defects thereof), O has the largest valence orbital cross section for $h\nu = 21.2\,\text{eV}$. This value has thus been used to estimate the lower limits of the defect concentration.
[58] D. Ricci, C. Di Valentin, G. Pacchioni, P. V. Sushko, A. L. Shluger, and E. Giamello, J. Am. Chem. Soc. **125**, 738 (2003).
[59] M. Sterrer, T. Berger, O. Diwald, E. Knozinger, P. V. Sushko, and A. L. Shluger, J. Chem. Phys. **123**, 064714 (2005).
[60] P. V. Sushko, A. L. Shluger, K. Hayashi, M. Hirano, and H. Hosono, Phys. Rev. B **73**, 014101 (2006).
[61] S. Sallis, K. T. Butler, N. F. Quackenbush, D. S. Williams, M. Junda, D. A. Fischer, J. C. Woicik, N. J. Podraza, B. E. White, A. Walsh, and L. F. J. Piper, Appl. Phys. Lett. **104**, 232108 (2014).
[62] S. Sallis, N. F. Quackenbush, D. S. Williams, M. Senger, J. C. Woicik, B. E. White, and L. F. J. Piper, Phys. Status Solidi A **212**, 1471 (2015).